

Article

Structural Synergy of NanoAl₂O₃/NanoAl Composites with High Thermomechanical Properties and Ductility

Magzhan K. Kutzhanov ¹, Andrei T. Matveev ¹, Andrey V. Bondarev ², Igor V. Shchetinin ¹, Anton S. Konopatsky ¹ and Dmitry V. Shtansky ^{1,*}

¹ Research Laboratory "Inorganic Nanomaterials", National University of Science and Technology MISIS, Leninsky Prospekt 4, Moscow 119049, Russia; ingvar@misis.ru (I.V.S.); konopatskiy@misis.ru (A.S.K.)

² Bernal Institute, School of Engineering, University of Limerick, Limerick V94 T9PX, Ireland

* Correspondence: shtansky@shs.misis.ru

Abstract: Achieving a combination of high strength and ductility in metal-based composites is still a difficult task, and it is especially challenging in a wide temperature range. Here, nanoAl₂O₃/nanoAl composites with high tensile and compressive strength and excellent ductility at 25 and 500 °C were obtained using Al and Al₂O₃ nanopowders via a combination of high-energy ball milling (HEBM) and spark plasma sintering (SPS). Being about three times lighter than conventional high-strength steel (with a density of 2.7 g/cm³ vs. that of 7.8 g/cm³ for steel), the nanoAl₂O₃/nanoAl materials demonstrated tensile strength and elongation before failure comparable with those of steel. The nanoAl₂O₃/nanoAl composites were strengthened with two types of Al₂O₃ NPs, in situ formed, and introduced into the powder mixture. The resulting materials had a bimodal microstructure consisting of Al with micron and submicron grains surrounded by an Al/Al₂O₃ framework whose structural components were all in the size range of 20–50 nm. Among the studied compositions (0, 1, 2, 3, 4, 5, 10, and 20 wt.% of Al₂O₃), the Al-3%Al₂O₃ material showed the best thermomechanical properties, such as a tensile strength of 512 MPa and 280 MPa and a compressive strength of 489 MPa and 344 MPa at 25 and 500 °C, respectively, with an elongation to failure of 15–18%. These results show the promise of nanoAl₂O₃/nanoAl composites for use as small items in the automotive and aviation industries.

Keywords: metal–matrix composites; ball milling; spark plasma sintering; microstructure; tensile and compressive strength



Citation: Kutzhanov, M.K.; Matveev, A.T.; Bondarev, A.V.; Shchetinin, I.V.; Konopatsky, A.S.; Shtansky, D.V. Structural Synergy of NanoAl₂O₃/NanoAl Composites with High Thermomechanical Properties and Ductility. *Metals* **2023**, *13*, 1696. <https://doi.org/10.3390/met13101696>

Academic Editor: Barrie Mintz

Received: 25 August 2023

Revised: 29 September 2023

Accepted: 2 October 2023

Published: 5 October 2023



Copyright: © 2023 by the authors. Licensee MDPI, Basel, Switzerland. This article is an open access article distributed under the terms and conditions of the Creative Commons Attribution (CC BY) license (<https://creativecommons.org/licenses/by/4.0/>).

1. Introduction

Due to its low density (2.7 g/cm³), aluminum (Al) is increasingly replacing cast iron and stainless steel in various industrial applications. However, Al, as a structural material, is rarely used in its pure form, but it is the basis of many metal–matrix composite (MMC) materials, including those based on complexly alloyed matrices (such as Al alloys of the 2xxx, 3xxx, 6xxx, and 7xxx series). Dispersion hardening via adding poorly soluble ceramic nanoparticles (NPs), for example, Al₂O₃, is the traditional approach used to increase strength [1]. Using this approach, it is possible to achieve a decent room-temperature ultimate tensile strength (UTS) of 250–280 MPa in Al/Al₂O₃ [2,3] and 400–425 MPa in Al-2124/Al₂O₃ [4], Al-6061/Al₂O₃ [5], and Al-7075/Al₂O₃ [6] materials. The problem of weak Al/Al₂O₃ interface bonding that can lead to a decrease in strength was addressed by a creating roughened interface [7]. It is also important to note that the high tensile strength of Al–matrix composites (AIMCs), often achieved at room temperature, is already significantly reduced at 200 °C [8,9], which gives rise to the ambitious goal of improving thermomechanical properties of AIMCs to expand their applications.

The addition of heat-resistant NPs, for example, TiC_x [10] and (AlN + γ-Al₂O₃) [11], which are often distributed along the Al grain boundaries (GBs), prevents dislocation

glide and leads to an increase in high-temperature strength. The presence of an amorphous alumina skeleton between Al grains enhances GBs' efficiency as dislocation barriers, remarkably strengthens AlMCs, and provides room-temperature elongation values of 7–26% [12]. However, the crystallization of amorphous Al_2O_3 skeletons leads to the formation of small (~90 nm) $\gamma\text{-Al}_2\text{O}_3$ NPs, which adversely affects mechanical properties. The presence of a metal–ceramic framework around metal grains can lead to different material behaviors under tension and compression [13].

Reducing the size of reinforcing particles to the nanoscale (<100 nm) contributes significantly to increasing composite strength via effectively preventing the movement of dislocations and grain growth. It has been reported that an improvement in mechanical properties can be achieved even at a low content of NPs [14–16]. Reducing the grain size of a metal to the nanometer scale (the Hall–Petch effect) also leads to a significant increase in mechanical strength, but it is accompanied by a decrease in plasticity, which limits composite applications. An increase in the ductility of an Al alloy with almost unchanged strength was observed when relatively large metal grains were present simultaneously with nanosized ones [17]. This observation led to the hypothesis that by combining a nanostructured material with high strength and micron-sized grains with high ductility, it is possible to obtain a composite with both high strength and ductility. It has been shown that with an increase in the volume fraction of large grains in nanostructured Al alloys, the alloys' strength decreases slightly, but their ductility increases markedly [18]. This behavior is explained by the formation of a bimodal microstructure, since grains of different sizes have the same composition. The concept of a bimodal microstructure of materials with high strength and ductility was further confirmed through the development of a trimodal microstructure in an Al alloy. Compared to a bimodal one, the trimodal material had twice the mechanical strength (~1060 MPa at room temperature), although its ductility was significantly lower: it presented a strain-to-failure value of 2.5% compared to that of 14% in the bimodal material [19]. Thus, these results indicate that a balance between strength and ductility can be achieved through microstructure design. It is worth noting that with increasing temperature, the strength of Al-5083 alloy with a trimodal microstructure dropped sharply. This behavior is a typical precipitation-hardening mechanism when precipitates are dissolved at elevated temperatures. Therefore, to create a material with both high strength and ductility at high temperatures, it is necessary to obtain dispersion-strengthened composites with multimodal microstructures. For example, researchers have achieved high strength yet enhanced ductility of AlMCs through the formation of a heterogeneous microstructure in which Al grains were separated by a nanocrystalline ceramic-reinforced Al matrix [13].

Although moderate strengthening can be achieved using large, micron-sized particles [20], the most pronounced strengthening effect is observed when using a few volume percentage of ceramic NPs (usually <5 vol.%) with a size of less than 50 nm [15,16]. However, achieving a uniform distribution of a small number of ultrafine particles is a difficult task. In addition, the synthesis of particles of a nanometric and uniform size or the separation of a narrow fraction from a powder significantly increases production costs. This suggests that the use of a nanopowder with a wide size distribution of NPs may have a certain advantage.

The aim of this work was to obtain nano Al_2O_3 /nanoAl composites with high strength and ductility due to the formation of a multimodal microstructure. To achieve this, unfractionated nanopowders of aluminum and aluminum oxide with a wide particle size distribution, namely, in the range of 10–500 nm, with a maximum number of NPs having a size of less than 200 (Al) and 100 nm (Al_2O_3), were used. The advantage of using Al NPs is the presence of oxide shells on their surfaces, which prevents their coalescence during mechanical processing [21]. To obtain high mechanical properties, a uniform distribution of ceramic NPs in a metal matrix is required. This was achieved using the high-energy ball milling (HEBM) of powder mixtures. The nano Al_2O_3 /nanoAl composites were prepared using HEBM and subsequent spark plasma sintering (SPS). The obtained materials were

thoroughly characterized using high-resolution transmission electron microscopy (HRTEM) and tensile and compression tests at 25 and 500 °C. Our strategy is based on the hypothesis that nanoAl₂O₃/nanoAl composites can be granted excellent thermomechanical properties through a combination of three mechanisms: Al grain size stabilization, the creation of an oxide framework along Al grain boundaries, and dispersion strengthening with Al₂O₃ NPs and other ceramic byproducts.

2. Experiments

NanoAl₂O₃/nanoAl composites were prepared using Al and Al₂O₃ nanopowders. Al nanopowder was produced from Al wire with a purity of 99.8% by exploding it with electrical current in an oxygen-containing atmosphere (OOO Equilibrium, Saransk, Russia). Al₂O₃ powder was produced via the evaporation of Al nanopowder (purity 99.5%) in an induction air–oxygen plasma followed by vapor condensation (Plasmotherm, Moscow, Russia). The size and morphology of the starting materials were determined via scanning electron microscopy (SEM) using a JSM-7600F microscope (JEOL, Tokyo, Japan). The particle size distribution was determined using ImageJ software (version 1.54t, Fiji).

The initial powder mixtures with different Al₂O₃ proportions (0, 1, 2, 3, 4, 5, 10, and 20 wt.%) were dry-processed in an E_{max} HEBM (Retsch GmbH, Haan, Germany). The ball-to-powder weight ratio was 10:1, and the rotation speed was 400 rpm. To minimize oxidation during mixing, the grinding jars were filled with argon. The total mixing time was 3 h. Every 30 min, the treatment was stopped, and the jar walls were cleaned of adhering powder to improve homogenization of the mixture. The jars were opened in a box filled with argon and kept this way for 30 min to prevent a fast reaction with air. Then, the adhered powder was removed from the jar walls in air; after that, the jar was again refilled with argon, and HEBM was continued.

The SPS method was used to consolidate the nanoAl₂O₃/nanoAl powder mixtures. Sintering was carried out using a Labox 650 setup (SINTER LAND Inc., Niigata, Japan). At the beginning of the process, a uniaxial pressure of 50 MPa was applied to the powder mixture, after which the sample was heated in two stages under vacuum (40 Pa). First, the powder mixture was heated to 300 °C with isothermal holding time of 10 min to remove absorbed impurities, and in the second stage, the sample was sintered at a temperature of 630 °C with a holding time of 10 min. Also, under the same HEBM and SPS conditions, a reference sample was obtained from the Al nanopowder to which Al₂O₃ NPs were not added. Samples with 0, 1, 2, 3, 4, 5, 10, and 20 wt.% of Al₂O₃ are denoted as Al-0, Al-1, Al-2, Al-3, Al-4, Al-5, Al-10, and Al-20.

The microstructure and morphology of the initial Al and Al₂O₃ nanopowders were analyzed via X-ray diffraction (XRD) using a DRON-3 (Burevestnik, Saint Petersburg, Russia) and via scanning electron microscopy (SEM) using a JSM F7600 instrument (JEOL Ltd., Tokyo, Japan). The microstructure of composite materials was examined via XRD and transmission electron microscopy (TEM) using a Titan Themis³ microscope (FEI, Eindhoven, The Netherlands) operated at 300 kV and equipped with an energy-dispersive X-ray spectroscopy (EDS) Super-X Detection System and by using a Tecnai TF20 X-Twin microscope (FEI, Eindhoven, The Netherlands). TEM sample preparation procedure was performed by means of the FIB technique using dual-beam Helios system with Ga⁺ liquid metal ion source (FEI, Brno, Czech Republic).

Tensile and compressive properties at room temperature (RT) and 500 °C were measured using an AG-X 20 kN universal testing machine (Shimadzu, Tokyo, Japan) equipped with a high-temperature furnace. The strain rates of tension and compression were 0.83×10^{-4} m/s and 1.16×10^{-5} m/s, respectively. To carry out high-temperature tests, the samples were placed in the furnace of the testing machine and kept in the heated zone for two minutes. Throughout the entire test cycle, the temperature in the heating zone and the sample temperature were controlled using thermocouples. The strain values were calculated, taking into account the calibration stiffness of the setup, which was determined on standard aluminum samples. Test specimens were cut on a CHMER GX-320L electric spark wire cutter (CHMER EDM, Hangzhou, China). For tensile tests, the specimens were shaped into a dumbbell 28–32 mm long and with a 5 mm long constriction and a cross-sectional area of 1.5×4 mm². For compression tests, the

specimens were formed into rectangular bars with dimensions of $4 \times 4 \times 8 \text{ mm}^3$. At least four measurements were conducted for each sample. Microhardness (Vickers pyramid number HV_5) measurements were carried out using an automatic microhardness tester Durascan 70 (Emco-test, Kuchl, Austria) by applying a load of 5 N for 15 s. Indentation was carried out at seven different random points on the composites' surfaces, and the results were average.

3. Results

3.1. Microstructure of Nano Al_2O_3 /NanoAl Composites

SEM images of the initial Al and Al_2O_3 nanopowders are presented in Figure 1a,b. The Al NPs are spherical in shape, and their size ranges from 25 to 500 nm, with most of the NPs being on the order of $\sim 80 \text{ nm}$ (Figure 1e). Their surface is covered with a thin amorphous layer of aluminum oxide/hydroxide $\sim 16 \text{ nm}$ thick, regardless of the particle size (Figure 1a(inset)). The results of the EDS analysis show that the Al NPs contain 86.5 at.% of Al and 13.3 at.% of O, corresponding to 17.7 wt.% of Al_2O_3 . The oxide layer in the Al NPs with a diameter of 80 nm is about 10.5 vol.%. The alumina NPs have a spherical shape with a size in the range of 10–500 nm, the predominant size observed among these nanoparticles is approximately 40 nm (Figure 1f). Figure 1c,d represent the XRD patterns of the Al and Al_2O_3 NPs. In addition to the main metal component, low-intensity peaks from Al_2O_3 are visible in the XRD pattern of the Al powder. Alumina in the Al_2O_3 nanopowder is present in three structural components: 70.1% of $\delta\text{-Al}_2\text{O}_3$ (ICDD card 00-056-1186), 15.2% of $\alpha\text{-Al}_2\text{O}_3$ (ICDD card 00-050-1496), and 14.7% of $\gamma\text{-Al}_2\text{O}_3$ (ICDD card 01-074-46290).

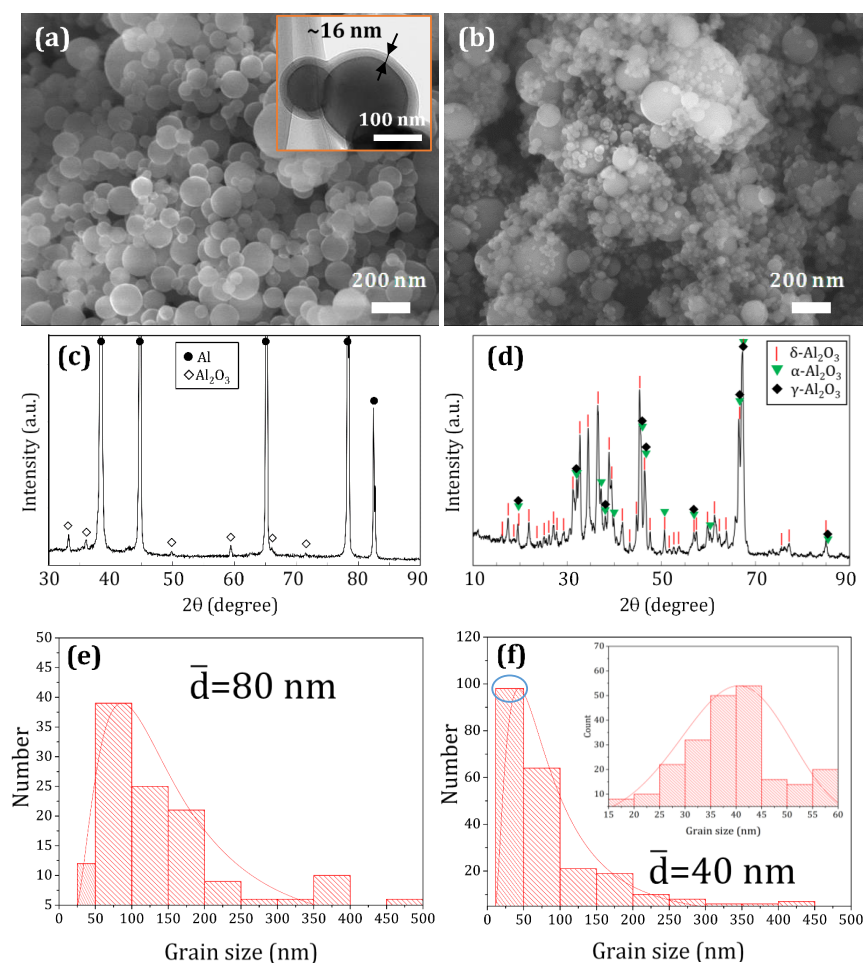


Figure 1. SEM images of the initial Al (a) and Al_2O_3 (b) nanopowders and particle size distributions: Al (e) and Al_2O_3 (f). Oxide layer on the surface of Al particles (inset in (a)). X-ray diffraction patterns of Al (c) and Al_2O_3 (d) nanopowders.

The microstructure of the Al-3 powder mixture is shown in Figure 2. It can be seen that, after HEBM, the nanoparticles largely retain their size and spherical morphology. The presence of a thin alumina layer on the surface of Al NPs prevented their agglomeration. Occasionally, two Al NPs fused together to form a dumbbell-shaped agglomerate (Figure 2b). The EDS oxygen map shows that the interface between the Al NPs is enriched with oxygen, as indicated by the dotted lines in Figure 2c. It is worth noting that due to localized heating during HEBM, the outer layer of the amorphous oxide shell can crystallize, typically within a range of 3 to 4 atomic layers.

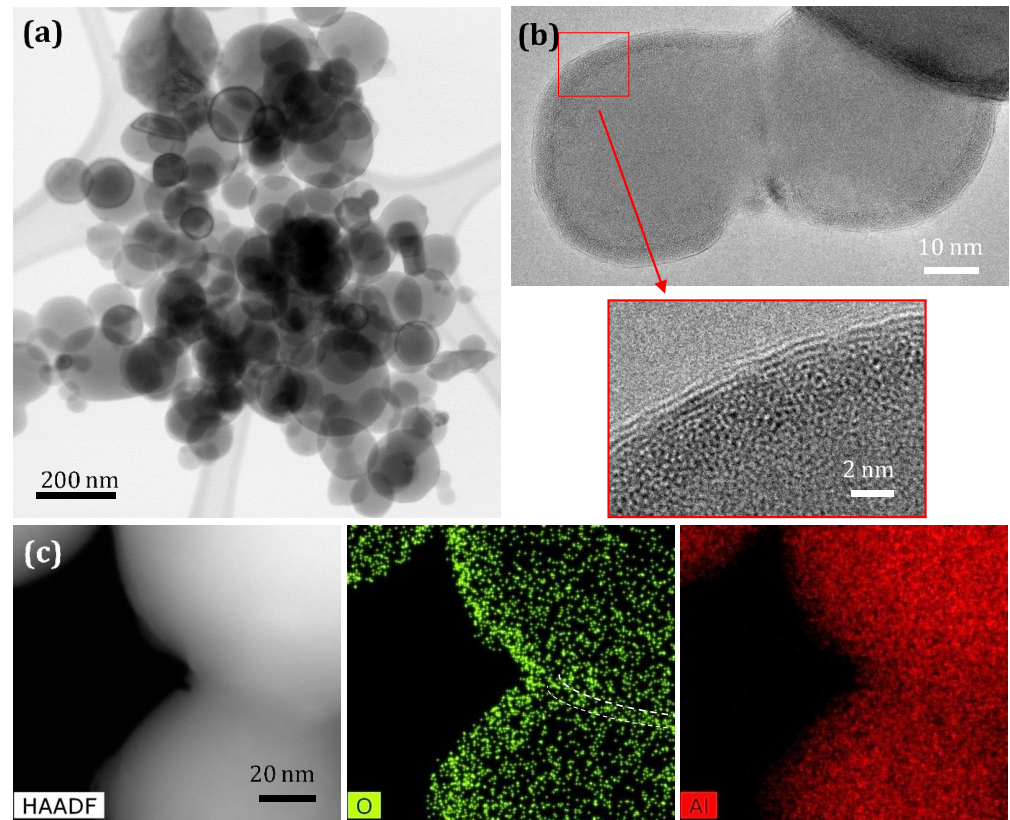


Figure 2. SEM (a) and TEM (b) images of Al-3 powder mixture after HEBM. Two merged dumbbell-shaped Al NPs with corresponding EDS elemental maps (c). The dotted lines indicate the oxygen-enriched particle fusion region.

The bimodal microstructure of sample Al-3 after SPS is shown in Figure 3a. In the image, submicron Al grains are surrounded by a finely dispersed composite structure consisting of nanosized Al grains and high amounts of ceramic inclusions. According to the XRD pattern, Al is the main phase in the composite. The 2θ regions of increased intensity to the left and right of the Al peaks can be attributed to contributions from the orthorhombic Al_2O_3 phase (Figure 3b). Weak signals from aluminum nitride can also be observed. The selected area electron diffraction (SAED) patterns reveal individual characteristic reflections from the (111) and (013) planes of the orthorhombic Al_2O_3 and (101) and (112) planes of trigonal Al_2O_3 (mp-1143, $R\bar{3}c$) (Figure 3c,d). Single reflections from the (100) planes of AlN are also visible (Figure 3c). The presence of Al_2O_3 and AlN nanoparticles was also confirmed through high-resolution TEM imaging and the corresponding SAED patterns (Figure 3e,f). The spherical inclusions are the Al_2O_3 reinforced NPs, while the AlN NPs have a characteristic faceting and a size of 35–125 nm. Since Al_2O_3 powder was produced via the evaporation of Al nanopowder in an induction air–oxygen plasma, it is reasonable to assume that this also led to the formation of amorphous AlN_xO_y nanoparticles [22], which

cannot be identified via XRD (Figure 1d). During the SPS process, amorphous AlN_xO_y nanoparticles can easily interact with Al according to the following reaction:

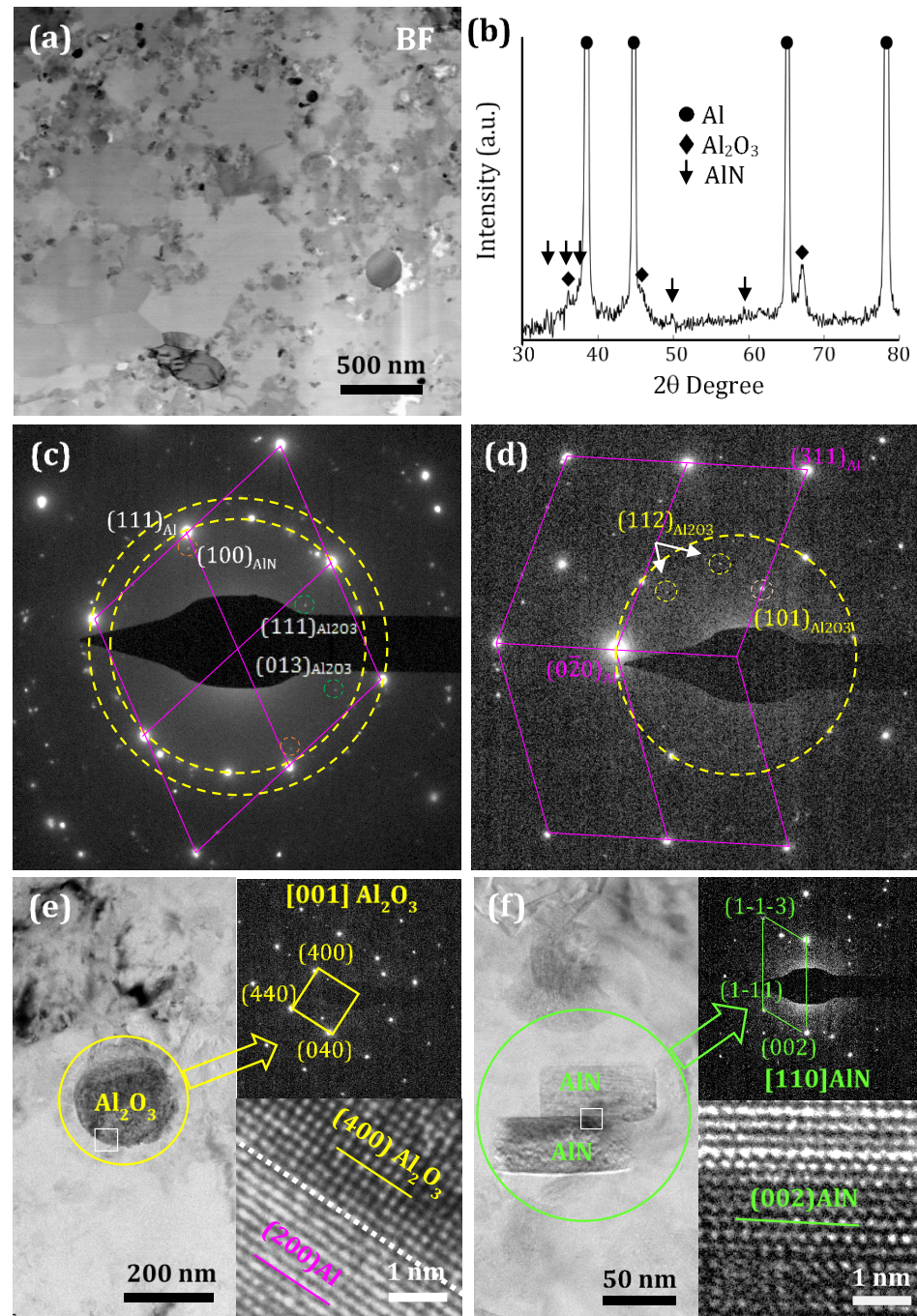
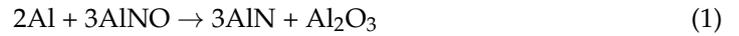


Figure 3. Bright-field TEM image (a) and XRD pattern (b) of sample Al-3 after HEBM and SPS. Selected area electron diffractions (SAED) along $[0\bar{1}1]_{\text{Al}}$ (c) and $[10\bar{3}]_{\text{Al}}$ (d) zone axes. TEM, high-resolution TEM, and SAED patterns showing Al_2O_3 (e) and AlN (f) nanoparticles.

This explains the formation of AlN nanoparticles in the Al/ Al_2O_3 composites prepared using SPS, similar to what was observed in the in-situ reaction between Al and amorphous SiN_xO_y [23].

The nanoAl₂O₃/nanoAl composite structure was further studied using the STEM technique and corresponding EDS Al, O, and N mapping. It can be seen that a submicron-sized Al grain (G1) is surrounded by oxygen-rich compounds that form a 3D oxide skeleton (Figure 4). Two characteristic morphologies of the oxide NPs can be distinguished. The spherical NPs are reinforcing Al₂O₃, which was originally part of the green Al-Al₂O₃ powder mixture (shown by arrows) (Figure 4). Shapeless NPs, which were closely spaced or adjacent to each other, forming an oxide network, apparently formed from an amorphous/crystalline surface oxide layer covering the initial Al NPs during SPS. As indicated by the results of the EDS and XRD analyses, a minor quantity of AlN NPs is also detected as a reinforcing phase.

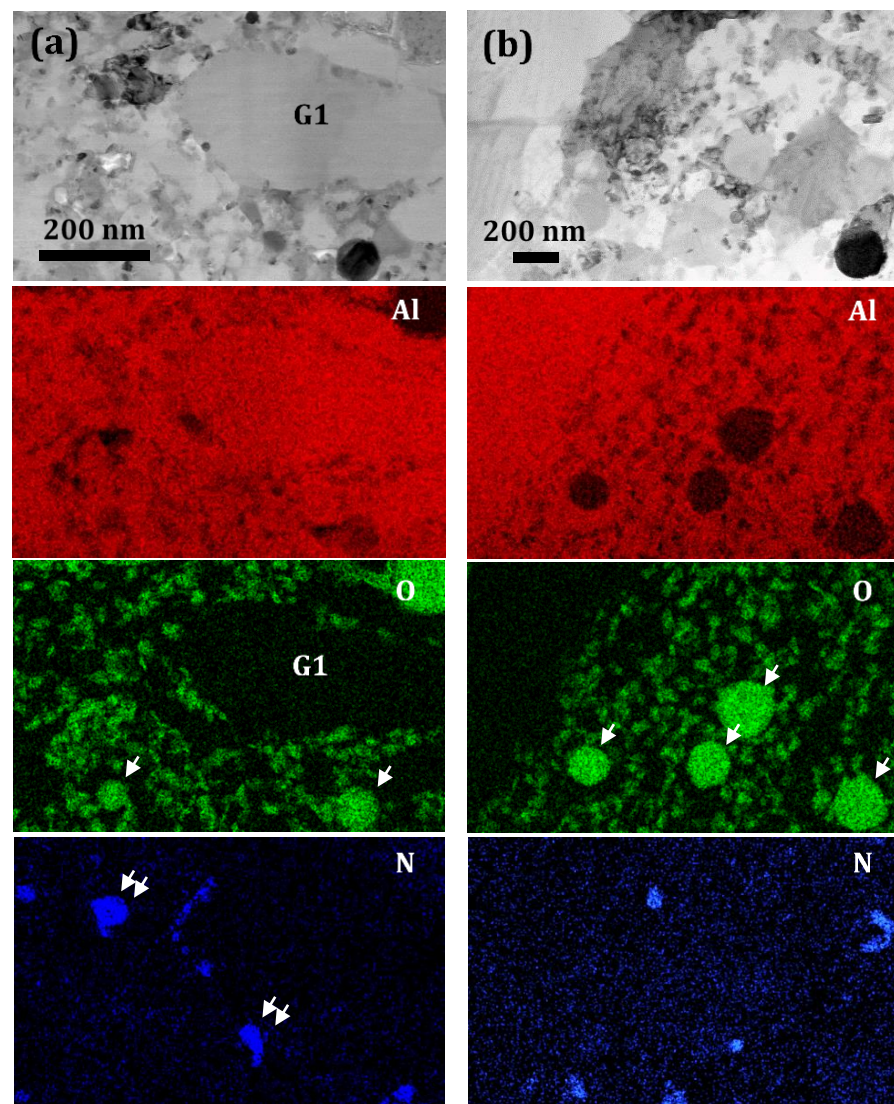


Figure 4. Bright-field STEM images of sample Al-3 (a,b) and corresponding EDS elemental maps. Spherical NPs included in the initial Al-Al₂O₃ powder mixture are indicated by arrows. Double arrows indicate the formed AlN nanoparticles.

Figure 5a,b show bright- and dark-field (BF and DF) STEM micrographs of an individual Al grain that was sufficiently well aligned along a $\langle 1\bar{1}0 \rangle$ zone axis. The grain has dimensions of approximately $380 \times 550 \text{ nm}^2$ and contains many microstructural defects. The Al grain is surrounded by oxide NPs, which lie in and below the image plane and are clearly visible on the corresponding EDS oxygen map. Figure 5c depicts an Al/Al₂O₃ interface tilted to the image plane. The (025)_{Al₂O₃} planes exhibit a precise alignment with

the $(200)_{\text{Al}}$ planes across the interface, forming a coherent grain boundary (as they have the same interplanar spacing of 0.202 nm).

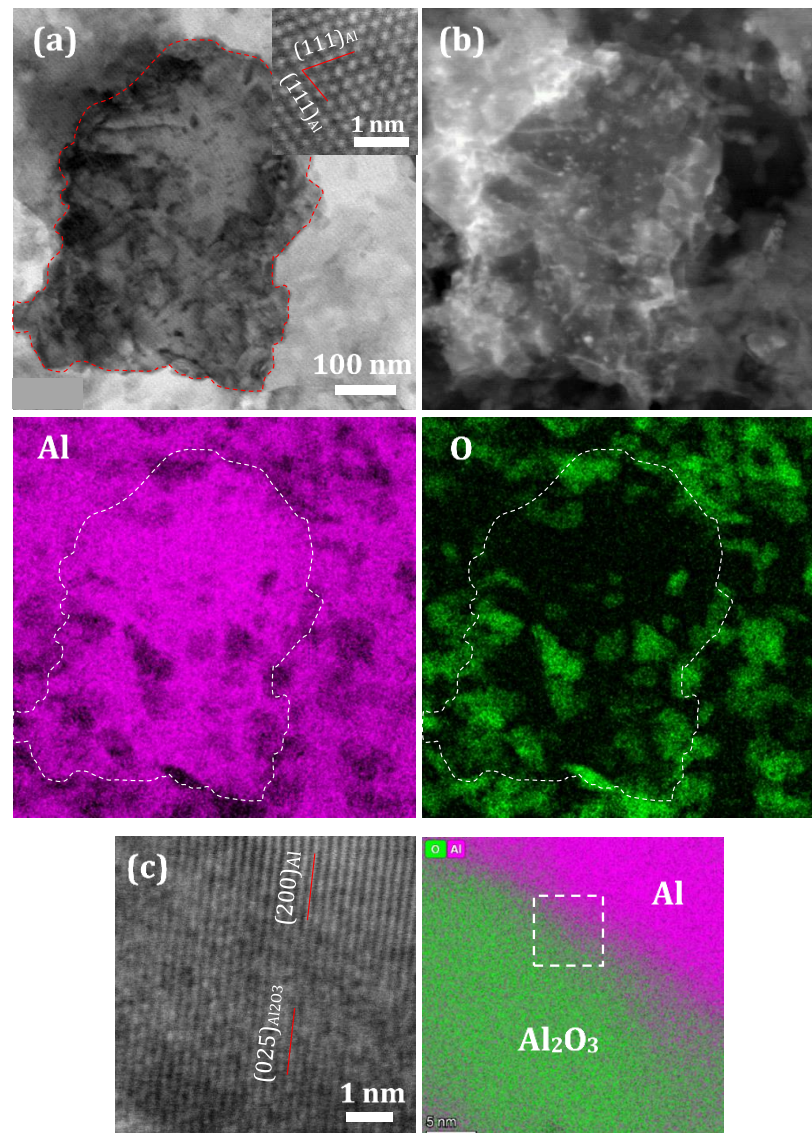


Figure 5. BF with HAADF (inset) (a) and DF (b) STEM images of Al grain (zone axis is $[110]$) and corresponding EDS Al and O maps. High-resolution BF STEM image (c) and corresponding EDS elemental map showing a coherent Al/ Al_2O_3 interface. The $(025)_{\text{Al}_2\text{O}_3}$ planes ($d = 0.202$ nm) are perfectly matched through the interface with the $(200)_{\text{Al}}$ planes ($d = 0.202$ nm).

The microstructure of the nano Al_2O_3 /nanoAl composite after the room-temperature (RT) tensile tests is presented in Figure 6. The TEM images reveal the types of defects that have developed within the material during deformation. Figure 6a–c show dislocations localized inside 600–700 nm Al grains. These dislocations were arrested by grain boundaries, ensuring their high density ($\sim 3.5 \times 10^{13} \text{ m}^{-2}$). The dislocations are well aligned in certain directions, which indicates that they were formed during plastic deformation along the planes of the easiest shear and not as a result of the accommodation of thermal stresses between the Al grain and the surrounding Al oxide NPs. Figure 6d displays a dark-field TEM micrograph of an individual Al grain approximately 300 nm in size aligned along the $\langle 01\bar{1} \rangle$ zone axis. Inside the grain, a high density of dislocations can be observed, among which dislocation loops and stacking faults formed exclusively along close-packed (111) planes can be distinguished (Figure 6e).

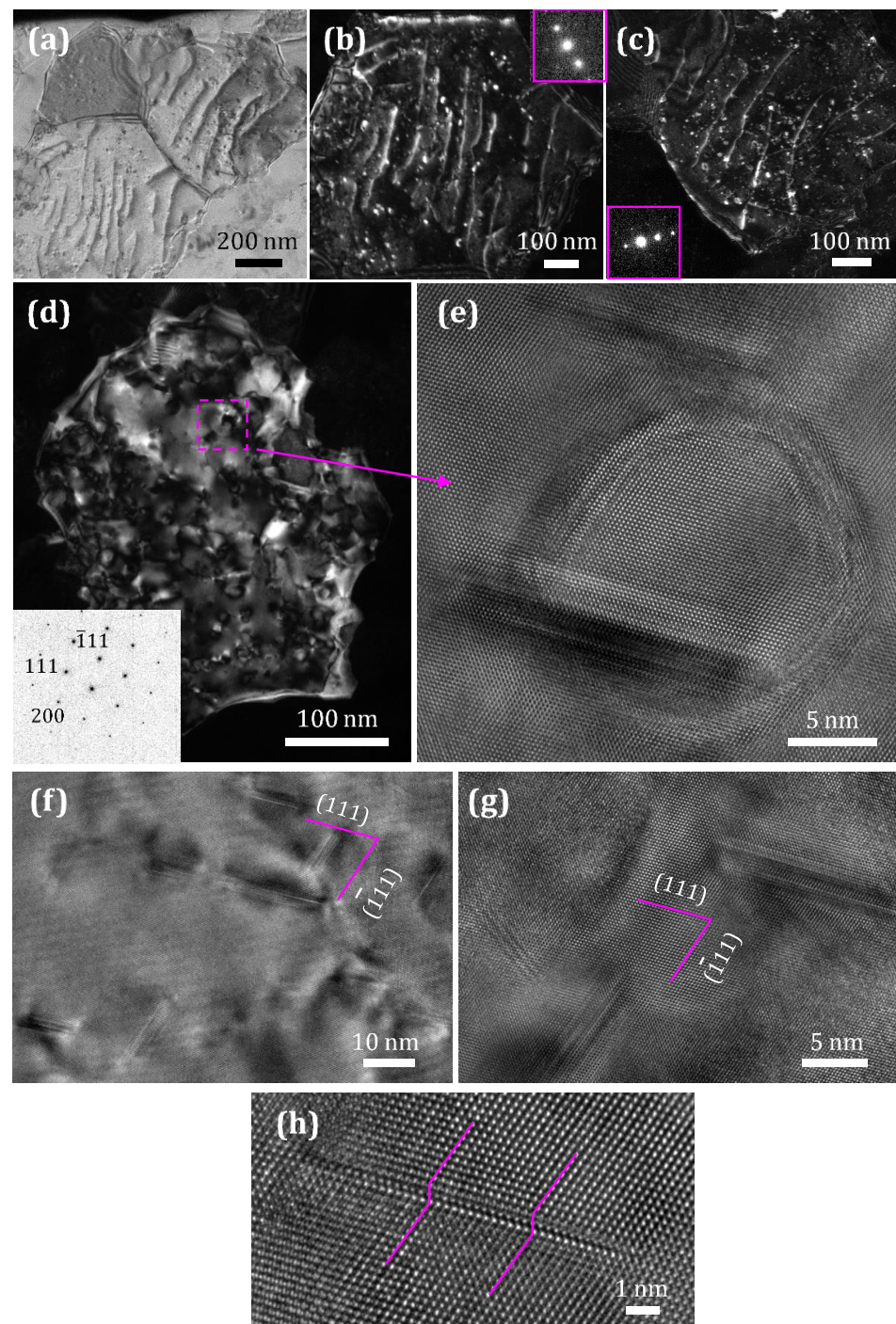


Figure 6. NanoAl₂O₃/nanoAl composite after RT tensile test. Bright- (a) and weak-beam dark-field (b,c) TEM images showing long dislocations localized inside Al grains after deformation. Dark-field TEM image of an Al grain (d), and high-resolution TEM image of a dislocation loop intersecting with the SF (e). Incident beam is parallel to $[0\bar{1}1]_{\text{Al}}$. High-resolution TEM images of Al grains showing relatively wide (up to 3.5 nm (f,g)) and narrow (two atomic layers (h)) planar defects formed along close-packed $\{111\}$ planes. The densities of long dislocations and SFs are approximately 3.5×10^{13} and $1.5 \times 10^{15} \text{ m}^{-2}$.

Numerous dislocation loops are also visible as dark/bright diffuse circles in the BF/DF TEM images (Figure 7). Relatively wide (~3.5 nm) and narrow (two atomic layers) planar defects are present inside the metal matrix (Figure 6f–h). The contribution of reinforcing particles, bearing part of the applied load, can be demonstrated on an AlN NP as an example.

Figure 8 shows the dislocation network inside the AlN grain after tensile deformation at RT. Dislocations are mainly localized within one grain and do not extend beyond its boundaries.

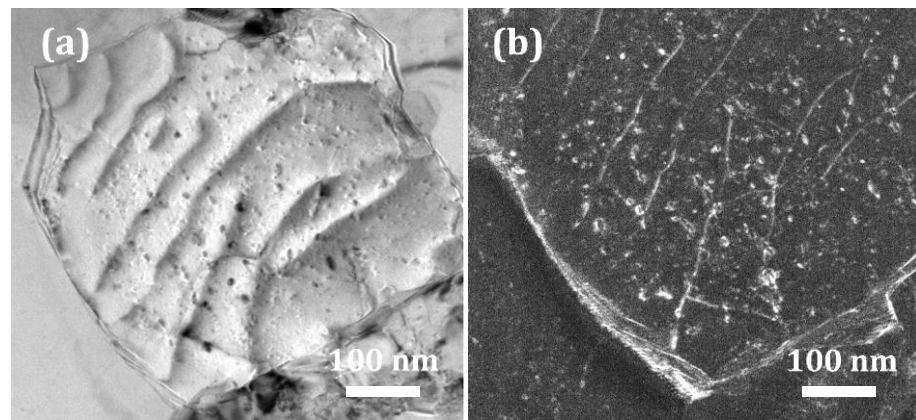


Figure 7. BF (a) and WBDF (b) TEM images of dislocation structure of Al grain after tensile test.

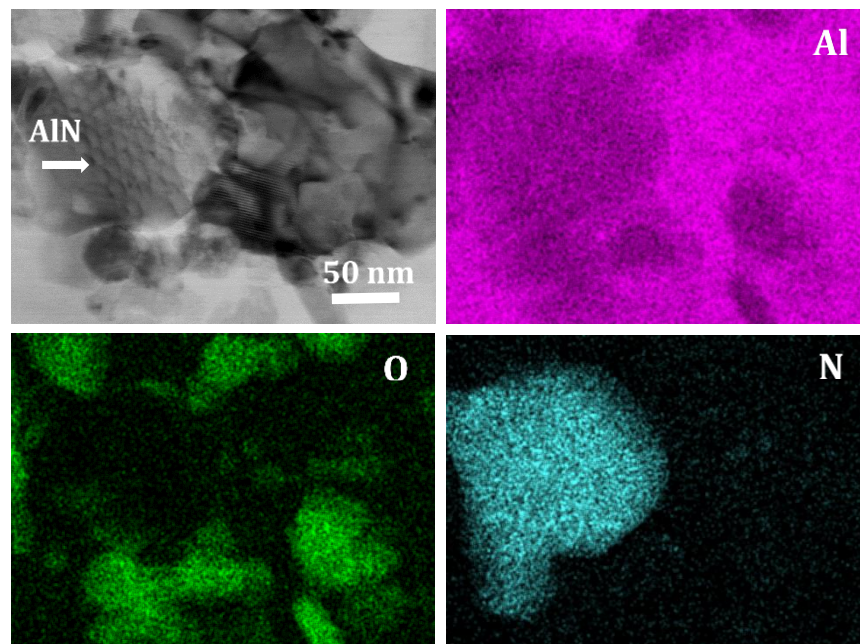


Figure 8. BF STEM image showing dislocation network in AlN after tensile deformation and corresponding EDS elemental maps.

3.2. Mechanical Properties of NanoAl₂O₃/nanoAl Composites at 25 and 500 °C

Figure 9 illustrates the relationship between the microhardness values of the composites and their respective densities. The reference sample, obtained exclusively from the Al nanopowder, has a hardness of 73 HV₅. As expected, with an increase in the alumina content, the hardness increases and reaches 154 HV₅ at 20 wt.% of Al₂O₃. Compared to the additive-free Al, the density gradually increases from 2.66 (Al-0) to 2.71 g/cm³ (Al-3), does not change much at 3–5 wt.% of Al₂O₃, and then increases to 2.76 (Al-10 and Al-20).

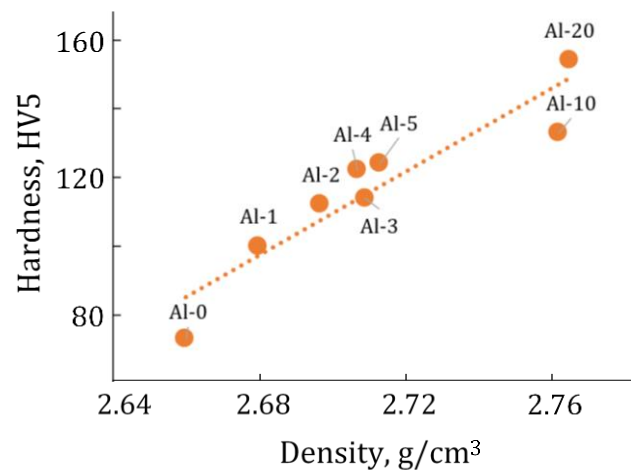


Figure 9. Microhardness of Al (Al-0) and nanoAl/nanoAl₂O₃ materials (Al-1–Al-20) vs. their density.

The average UTS and UCS values (MPa), as well as the elongations to failure (El, %), determined from the engineering tensile and compressive strength curves of the Al-nanopowder-derived reference samples and nanoAl₂O₃/nanoAl composites tested at 25 and 500 °C are presented in Table 1. The RT tensile strength increases starting from 194 MPa (Al), reaches a maximum of 512 MPa at 3 wt.% of Al₂O₃, and then decreases to 160 MPa at 20 wt.% of Al₂O₃ (Figure 10a). Compared to pristine Al, the UTS value of sample Al-3 increased 2.6 times. At 500 °C, this sample also shows a maximum UTS value of 280 MPa (an increase by a factor of 1.8). These high values of UTS were achieved at enhanced elongations of 17.9% (25 °C) and 15% (500 °C), which are only 28 and 18.5% less than those in the sample without alumina additives (Table 1).

Table 1. Mechanical properties of Al and nanoAl₂O₃/nanoAl composites.

Sample	Hardness (HV ₅)	Compressive Properties				Tensile Properties			
		RT		500 °C		RT		500 °C	
		UCS (MPa)	El (%)	UCS (MPa)	El (%)	UTS (MPa)	El (%)	UTS (MPa)	El (%)
Al-0	73 ± 8	178 ± 8	19.0 ± 1.1	100 ± 5	12.2 ± 1	194 ± 5	24 ± 0.8	153 ± 10	18.4 ± 1
Al-1	100 ± 9	434 ± 9	11.5 ± 1.1	272 ± 8	9.6 ± 1	389 ± 7	12.3 ± 0.2	253 ± 3	14.9 ± 0.2
Al-2	112 ± 5	466 ± 6	25.1 ± 1.0	366 ± 5	22.2 ± 2	396 ± 15	15.9 ± 1.6	256 ± 8	14.5 ± 0.8
Al-3	114 ± 5	489 ± 10	17.8 ± 1.8	344 ± 7	18.2 ± 0.8	512 ± 20	17.9 ± 2	280 ± 11	15.0 ± 0.7
Al-4	122 ± 8	432 ± 7	9.1 ± 0.7	324 ± 8	20.8 ± 1.1	362 ± 10	12.1 ± 1	252 ± 11	15.9 ± 0.4
Al-5	124 ± 4	442 ± 10	14.1 ± 1.2	295 ± 2	18 ± 0.5	360 ± 15	16.8 ± 1.3	245 ± 9	17.2 ± 0.6
Al-10	133 ± 7	526 ± 11	16.7 ± 1.9	315 ± 12	12.5 ± 0.8	356 ± 7	11.9 ± 1.1	206 ± 3	13.2 ± 0.1
Al-20	154 ± 10	518 ± 8	4.8 ± 1	299 ± 10	4.3 ± 0.4	160 ± 5	5.2 ± 0.9	93 ± 3	7.8 ± 0.2

The characteristic engineering compressive strength curves of the Al and Al/Al₂O₃ samples tested at 25 and 500 °C are presented in Figure 10c,d. The dependence of compressive strength on the Al₂O₃ content does not have a pronounced maximum (Figure 10b). The RT UCS values increase from 178 MPa (Al) to 489 MPa (Al-3), slightly decrease at 4 and 5 wt.% of Al₂O₃ (samples Al-4 and Al-5), and then increase again at higher Al₂O₃ NP proportions (10 and 20 wt.%). At a testing temperature of 500 °C, the UCS exhibits a notable increase from 100 MPa (Al-0) to 366 MPa (Al-2). Subsequently, there is a slight decrease, with the UCS stabilizing at approximately 300 MPa for Al₂O₃ concentrations ranging from 4% to 20 wt%. Thus, compared to pure Al, the maximum increase in strength at 500 °C was 266%. However, in addition to a significant increase in compressive strength, the result that perhaps is even more crucial is the increase in ductility. For sample Al-2, the increase in elongation at RT was 44%. The nanoAl₂O₃/nanoAl composites with 2–5 wt.% of Al₂O₃ were 42–89% more ductile compared to the Al-0 material without Al₂O₃ additive (Table 1).

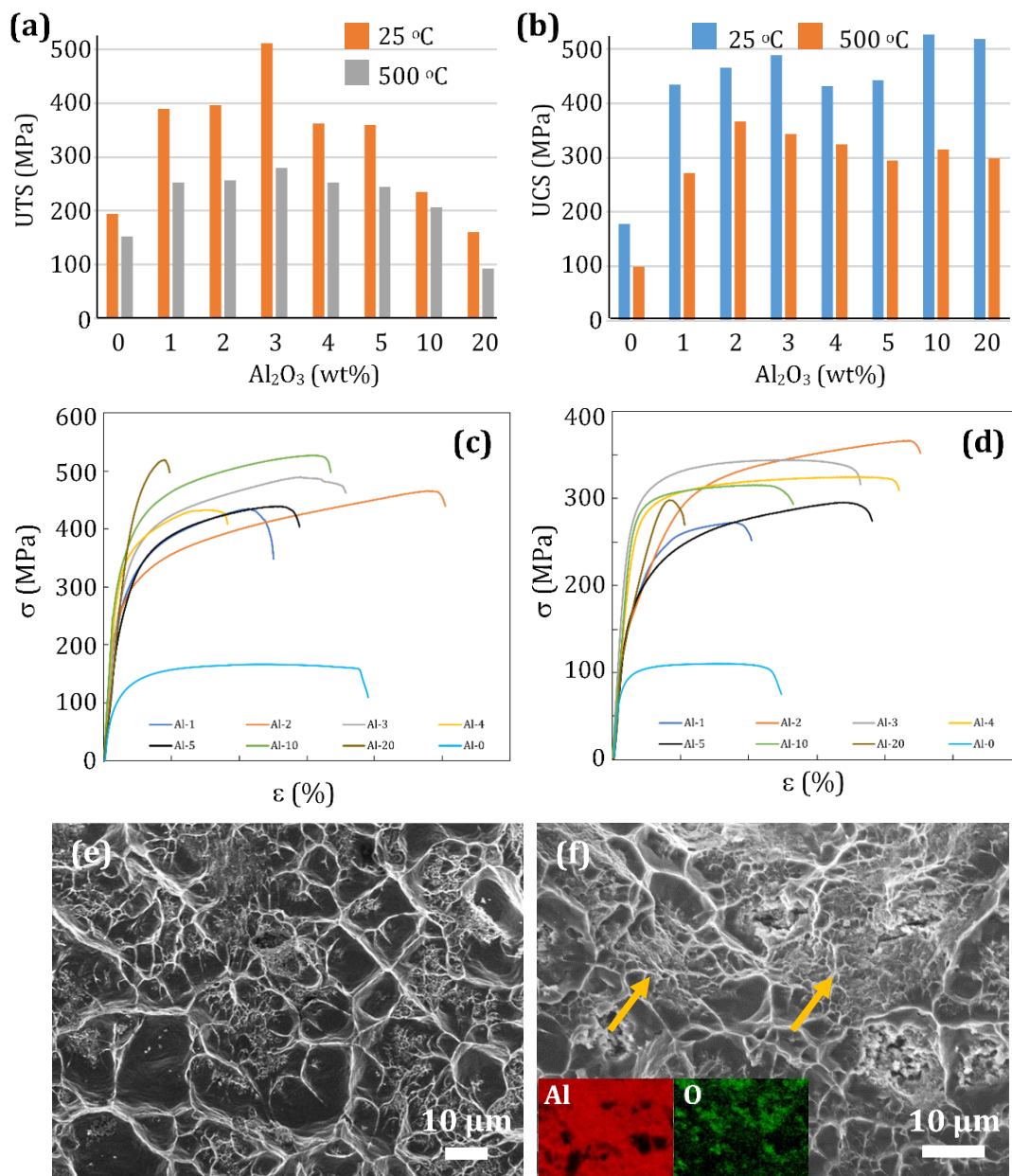


Figure 10. UTS (a) and UCS (b) values of Al and nanoAl₂O₃/nanoAl composites. Characteristic engineering compressive strain–stress curves of Al and Al/Al₂O₃ samples tested at 25 °C (c) and 500 °C (d). Al-0 (Al), Al-1 (Al-1%Al₂O₃), Al-2 (Al-2%Al₂O₃), Al-3 (Al-3%Al₂O₃), Al-4 (Al-4%Al₂O₃), Al-5 (Al-5%Al₂O₃), Al-10 (Al-10%Al₂O₃), and Al-20 (Al-20%Al₂O₃). SEM fracture images of sample Al-3 after tensile tests at 25 °C (e) and 500 °C (f). Arrows indicate oxygen-enriched areas, which exhibit a tendency toward more brittle fractures.

The high plasticity of the nanoAl₂O₃/nanoAl composites was confirmed by the appearance of sample surface fractures after mechanical tests. SEM fracture micrographs of composite Al-3 after RT and high-temperature tensile tests are presented in Figure 10e,f. The fracture surfaces have characteristic dimpled areas, indicating a predominantly plastic nature of deformation. It can be seen that regions with a relatively large cellular structure alternate with regions with a much finer structure, and this result is in good agreement with the bimodal microstructure of the nanoAl₂O₃/nanoAl composites (Figure 3a). The EDS elements maps show oxygen-enriched areas that exhibit a more brittle fracture pattern.

4. Discussion

Based on the results obtained, the following scheme for the formation of the composite nanoAl₂O₃/nanoAl structure was proposed. The initial Al NPs are covered with a layer of amorphous oxide/hydroxide (Al(OH)₃). Although during HEBM the Al nanopowder is subjected to severe deformation, the particles retain their initial size and spherical shape due to the protective oxide shell (Figures 2a and 11a). These amorphous shells also prevent Al grain growth during subsequent heating and SPS. Plasma breakdown during SPS additionally heats and destroys the amorphous layer, turning it into discrete crystalline Al₂O₃ NPs surrounding metal grains (Figure 11a). A similar microstructure was observed in a composite obtained from only Al nanopowder, in which reinforcing γ -Al₂O₃ NPs were formed from an amorphous oxide/hydroxide layer covering the initial Al NPs [24]. The formation of an alumina skeleton was also observed in the Al/Al₂O₃ composites [12]. The transformation of an amorphous alumina surface layer into crystalline Al₂O₃ was reported to occur during heating above 450 °C [25], and only nanometric γ -Al₂O₃ particles with an average size of 28 nm residing on the high-angle grain boundaries were observed after annealing at 600 °C for 24 h [26]. Therefore, it can be assumed that, in our case, Al₂O₃ NPs were formed not only as a result of spark breakdown but also during heating to 630 °C during SPS.

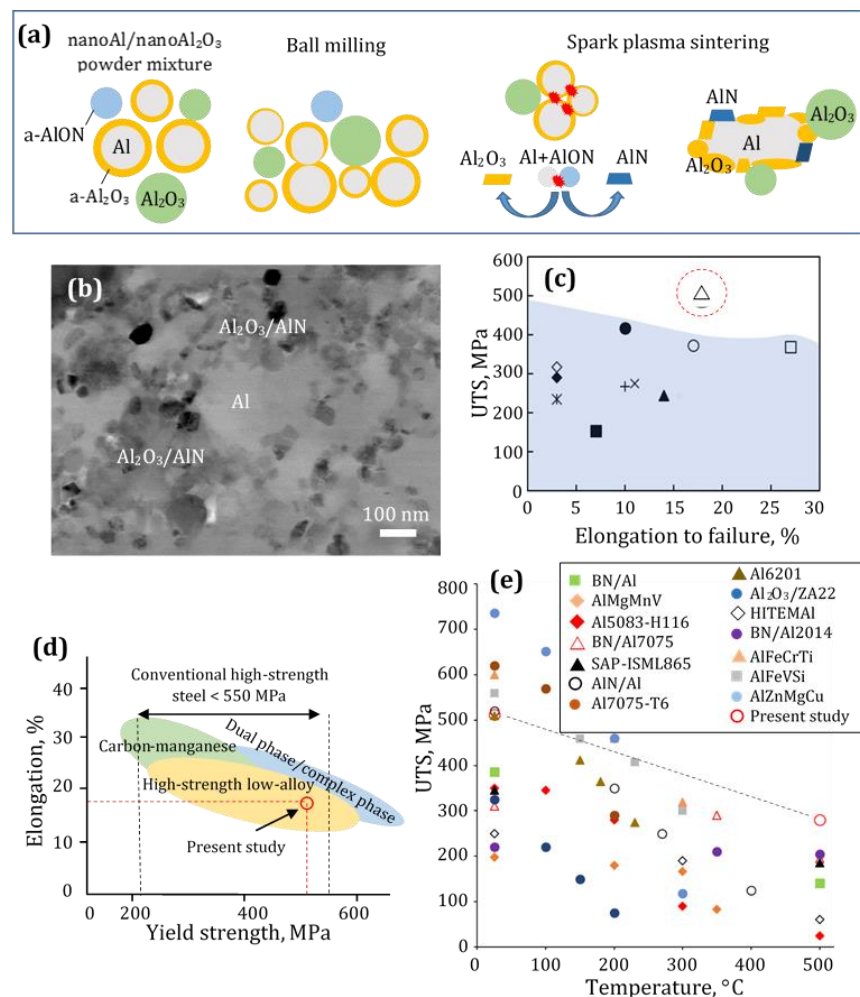


Figure 11. Schematics of nanoAl₂O₃/nanoAl composites' fabrication (a), BF TEM image showing bimodal microstructure (b), comparison of RT UTS and elongation values of various Al/Al₂O₃ composites (c) (+ [11], ◇ [25], ▲ [27], ○ [28], ◆ [29], ● [30], × [31], □ [32], * [33], ■ [34], △ present study), comparison of strength and elongation of Al-3 composite with those of conventional high-strength steels [35] (d), and comparison of UTS values of Al-3 composites at elevated temperatures with those of other materials (e) (data from Refs. [8,30,36–45]).

SEM images of samples Al-0, Al-3, and Al-10 with the corresponding distributions of Al grains by size are presented in Figure 12. It can be seen that, in addition to nano and submicron Al grains, the materials contain grains larger than 1 μm . Structural anisotropy can be observed, in which the Al grains are elongated perpendicular to the applied load. The formation of a bimodal microstructure with micron and submicron Al grains surrounding the (Al+Al₂O₃+AlN) nanocomposite is apparently due to the use of unfractionated Al nanopowder with a wide particle size distribution (Figures 11b and 12a–c). Thus, the nanoAl₂O₃/nanoAl composite was strengthened not only by the added Al₂O₃ NPs but also by the formed Al–ceramic skeleton with Al₂O₃ and AlN nano-inclusions surrounding micron and submicron Al grains.

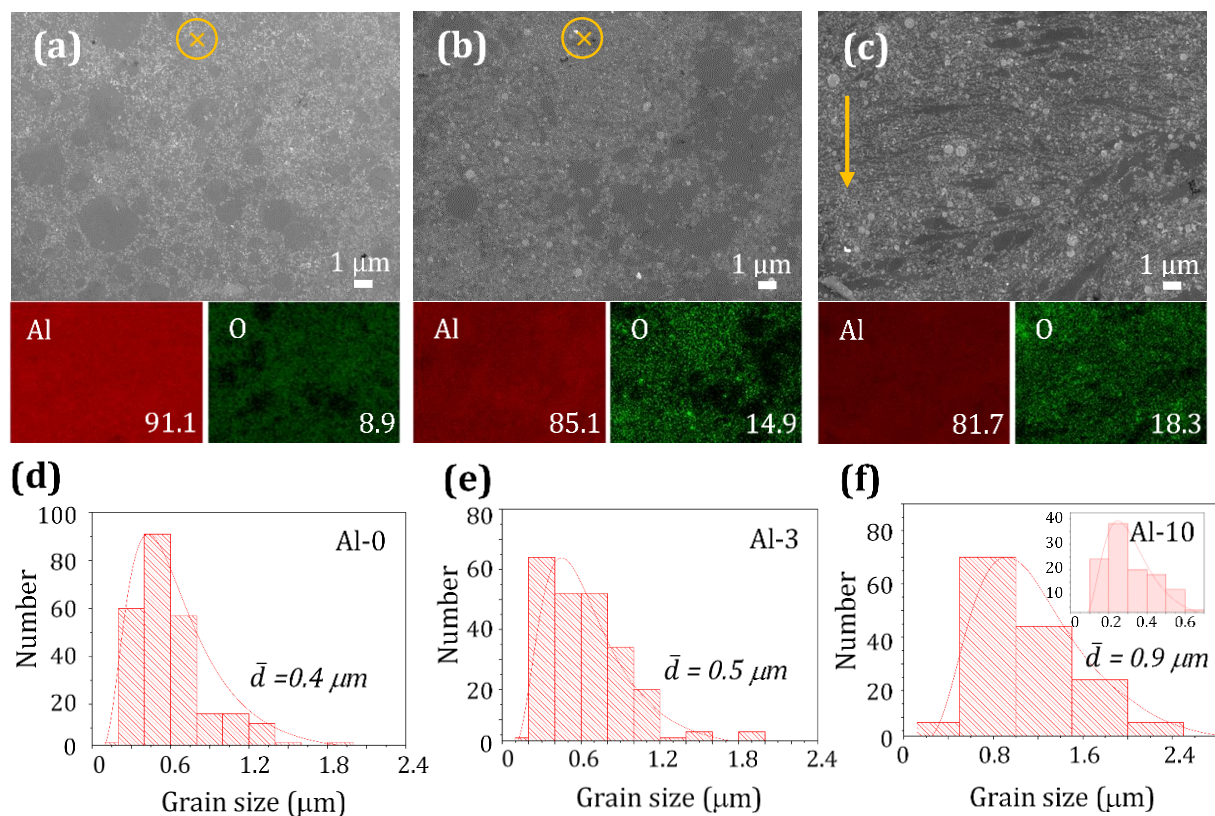


Figure 12. SEM images of Al/Al₂O₃ composites with corresponding EDS elemental maps and grain size distributions: Al-0 (a,d), Al-3 (b,e), and Al-10 (c,f). Samples Al-0 and Al-3 were cut perpendicular to the pressing direction, while sample Al-10 was cut along the pressing direction, as indicated by the arrow.

The nanoAl₂O₃/nanoAl material simultaneously shows high tensile/compressive strength and high ductility. This can be explained by the formation of a bimodal structure in which micron and submicron Al grains, responsible for plasticity, are encapsulated within a framework composed of Al nanograins and ceramic NPs, contributing to the material's strength. Figure 11c compares the UTS values of various Al/Al₂O₃ composites [11,25,27–34]. In terms of the combination of tensile strength and ductility, sample Al-3 outperforms many other Al/Al₂O₃ composites obtained so far. Its record strength of 512 MPa is significantly higher than the maximum strengths reported for Al-10%SiC (317 MPa) [46], Al-2%BN (405 MPa) [13], and Al-3%SiNO_x materials (395 MPa) [23]. The RT tensile strength and elongation of sample Al-3 are comparable with those of Al-7075 alloy subjected to T6 heat treatment [47], which is widely used in marine, automotive, and aircraft applications. Being about three times lighter than conventional high-strength steel (with a density of 2.7 g/cm³ vs. that of 7.8 g/cm³ for steel), the nanoAl₂O₃/nanoAl materials demonstrated tensile strength and elongation before failure comparable with

those of steel (Figure 11d) [35,48]. Our study clearly shows that the addition of an optimal quantity of Al_2O_3 NPs in the raw nanoAl powder is necessary to obtain record strength. Indeed, the Al-MCs reinforced only with in situ formed $\gamma\text{-Al}_2\text{O}_3$ nanoparticles displayed a compressive yield stress of 302 MPa and a ductility of 4% [21].

It is especially important to note the excellent mechanical properties of composite Al-3 at a temperature of as high as 500 °C: 344 MPa (in compression) and 280 MPa (in tension). For example, the UTS of Al-7075 alloy decreased to 40 MPa at 370 °C. Sample Al-3's tensile strength at 500 degrees is superior to that of many other metal–matrix composite materials (Figure 11e [8,30,36–45]). A nanoscale mixture of Al and in situ formed alumina NPs (Figure 4) surrounding Al grains ensures high compressive ductility, which was 1.32 (25 °C) and 1.82 (500 °C) times higher for sample Al-2 than for the pure Al-0 material (Table 1).

The study of the defect microstructure after deformation made it possible to shed light on the main strengthening mechanisms. Within the composite materials' microstructures, many Al grains are only a few hundred nanometers in size. Dislocations were observed within one grain without going beyond its boundaries (Figure 6a–c), leading to a high density and an increase in the number of microstresses and, consequently, strength. The increased plasticity observed can be explained by the fact that the dislocations do not cross the grain boundary and, apparently, angulate inside the grain. The Al_2O_3 and AlN NPs located along the Al grain boundaries limit the movement of dislocations and make an additional contribution to strengthening due to the creation of high-strain fields. In addition, ceramic NPs surrounding metal grains can prevent grain rotation or sliding (especially important for compression tests) and retard crack propagation. An important observation is that the AlN grains contain dislocations (Figure 8), indicating that the particles take on part of the mechanical load.

The numerous line defects and (111) microtwins/stacking (MTs/SFs) faults observed inside the Al grains also indicate metal plastic deformation (Figure 6e–h). This is in good agreement with the characteristic cellular microstructure of the composite fracture zone after tensile deformation (Figure 11c,d). Figure 6e shows that MTs/SFs act as barriers and traps for dislocations. This behavior can lead to an increase in strength and plasticity [49] as well as improved crack resistance due to stress relaxation [50].

The strength of the metal/ceramic interface bond is an important factor for the strength of the entire material. Long-term HEBM and subsequent SPS facilitate high bonding strength between Al and both in situ formed and doped Al_2O_3 NPs. A strong interface can be formed during the crystallization of thin amorphous Al oxide/oxyhydrate interlayers. The precipitation of extremely fine $\gamma\text{-Al}_2\text{O}_3$ NPs at the Al grain boundary leads to an order-of-magnitude enhancement in interface strength [51]. DFT calculations showed that the delamination of composites at the Al/ Al_2O_3 interface is unlikely to occur. After subjecting our composites to mechanical tests, we did not observe delamination or the appearance of cracks at the Al/ Al_2O_3 interfaces.

5. Conclusions

Nano Al_2O_3 /nanoAl composites with high strength and ductility at 25 °C and 500 °C were obtained from as-synthesized and non-fractionated Al and Al_2O_3 nanopowders through a combination of high-energy ball milling and spark plasma sintering. The nano Al_2O_3 /nanoAl material with the addition of 3 wt.% of the Al_2O_3 nanoparticles showed excellent thermomechanical properties both in terms of tension and compression. Compared with conventional cast Al (~80 MPa), the room-temperature tensile and compressive strength were increased by more than 500% to 512 MPa and 489 MPa, respectively. The nano Al_2O_3 /nanoAl material with 3 wt.% of Al_2O_3 retained a very high strength at 500 °C, i.e., approximately 280 MPa (tensile) and 340 MPa (compression), and showed an elongation to failure in the range of 15–18% under compression and tension both at 25 and 500 °C. The problem of a catastrophic decrease in plasticity with increasing strength was successfully solved by creating a bimodal composite microstructure containing micron and submicron Al grains, responsible for plasticity, sur-

rounded by a metal–ceramic skeleton (consisting of Al nanograins and ceramic nanoparticles), contributing to strength.

Author Contributions: M.K.K.—Data curation, Formal analysis, Investigation, and Writing—original draft. A.T.M.—Conceptualization, Investigation, and Writing—review and editing. A.V.B.—Investigation, Visualization, and Writing—review and editing. I.V.S.—Investigation. A.S.K.—Investigation. D.V.S.—Formal analysis, Resources, Writing—review and editing, and Supervision. All authors have read and agreed to the published version of the manuscript.

Funding: This research was funded by the Ministry of Education and Science of Russian Federation (FSME-2023-0004).

Data Availability Statement: The raw/processed data required to reproduce these findings cannot be shared at this time as the data also form part of an ongoing study. Some data can be made available upon request.

Conflicts of Interest: The authors declare no conflict of interest.

References

1. Koli, D.K.; Agnihotri, G.; Purohit, R. A Review on properties, behaviour and processing methods for Al-nano Al₂O₃ composites. *Proc. Mater. Sci.* **2014**, *6*, 567–589. [\[CrossRef\]](#)
2. Rezayat, M.; Akbarzadeh, A.; Owhadi, A. Production of high strength Al–Al₂O₃ composite by accumulative roll bonding. *Comp. Part A* **2012**, *43*, 261–267. [\[CrossRef\]](#)
3. Garbicz, D.; Jurczyk, M.; Levintant-Zayonts, N.; Mościcki, T. Properties of Al–Al₂O₃ composites synthesized by spark plasma sintering method. *Acrh. Civil Mech. Eng.* **2015**, *15*, 933–939. [\[CrossRef\]](#)
4. Dobrzański, L.A.; Włodarczyk, A.; Adamiak, M. The structure and properties of PM composite materials based on EN AW-2124 aluminum alloy reinforced with the BN or Al₂O₃ ceramic particles. *J. Mater. Process. Technol.* **2006**, *175*, 186–191. [\[CrossRef\]](#)
5. Oh, K.H.; Han, K.S. Short-fiber/particle hybrid reinforcement: Effects on fracture toughness and fatigue crack growth of metal matrix composites. *Compos. Sci. Technol.* **2007**, *67*, 1719–1726. [\[CrossRef\]](#)
6. Ezatpour, H.R.; Torabi Parizi, M.; Sajjadi, S.A.; Ebrahimi, G.R.; Chaichi, A. Microstructure, mechanical analysis and optimal selection of 7075 aluminum alloy based composite reinforced with alumina nanoparticles. *Mater. Chem. Phys.* **2016**, *178*, 119–127. [\[CrossRef\]](#)
7. Zhang, Z.; Fan, G.; Tan, Z.; Zhao, H.; Xu, Y.; Xiong, D.; Li, Z. Towards the strength-ductility synergy of Al₂O₃/Al composite through the design of roughened interface. *Comp. Part B* **2021**, *224*, 109251. [\[CrossRef\]](#)
8. Yu, S.; Li, W.; He, Z. Study on tensile strengths of Al₂O₃ short fiber reinforced Zn–Al alloy composites at elevated temperatures. *J. Antimicrob. Chemother.* **2007**, *431*, L8–L11. [\[CrossRef\]](#)
9. Wu, Y.-L.; Chao, C.-G. Deformation and fracture of Al₂O₃/Al–Zn–Mg–Cu metal matrix composites at room and elevated temperatures. *Mater. Sci. Eng. A* **2000**, *282*, 193–202. [\[CrossRef\]](#)
10. Wang, L.; Qiu, F.; Zhao, Q.; Zha, M.; Jiang, Q. Superior high creep resistance of in situ nano-sized TiC_x/Al–Cu–Mg composite. *Sci. Rep.* **2017**, *7*, 4540. [\[CrossRef\]](#)
11. Zan, Y.-N.; Zhou, Y.-T.; Li, X.-N.; Ma, G.-N.; Liu, Z.-Y.; Wang, Q.-Z.; Wang, D.; Xiao, B.-L.; Ma, Z.-Y. Enhancing high-temperature strength and thermal stability of Al₂O₃/Al composites by high-temperature pre-treatment of ultrafine Al powders. *Acta Metall. Sin. Engl. Lett.* **2020**, *33*, 913–921. [\[CrossRef\]](#)
12. Balog, M.; Krizik, P.; Nosko, M.; Hajovska, Z.; Victoria Castro Riglos, M.; Rajner, W.; Liu, D.-S.; Simancik, F. Forged HITEMAL: Al-based MMCs strengthened with nanometric thick Al₂O₃ skeleton. *Mater. Sci. Eng. A* **2014**, *613*, 82–90. [\[CrossRef\]](#)
13. Corthay, S.; Kutzhanov, M.K.; Matveev, A.T.; Bondarev, A.V.; Leybo, D.V.; Shtansky, D.V. Nanopowder derived Al/h-BN composites with high strength and ductility. *J. Alloys Compd.* **2022**, *912*, 165199. [\[CrossRef\]](#)
14. Zhang, Z.; Chen, D.L. Consideration of Orowan strengthening effect in particulate-reinforced metal matrix nanocomposites: A model for predicting their yield strength. *Scr. Mater.* **2006**, *54*, 1321–1326. [\[CrossRef\]](#)
15. Sanaty-Zadeh, A.; Rohatgi, P.K. Comparison between current models for the strength of particulate-reinforced metal matrix nanocomposites with emphasis on consideration of Hall–Petch effect. *Mater. Sci. Eng. A* **2012**, *531*, 112–118. [\[CrossRef\]](#)
16. Chen, X.-H.; Yan, H. Fabrication of nanosized Al₂O₃ reinforced aluminum matrix composites by subtype multifrequency ultrasonic vibration. *J. Mater. Res.* **2015**, *30*, 2197–2209. [\[CrossRef\]](#)
17. Tellkamp, V.L.; Lavernia, E.J.; Melmed, A. Mechanical behavior and microstructure of a thermally stable bulk nanostructured Al alloy. *Metall. Mat. Trans. A* **2001**, *32*, 2335–2343. [\[CrossRef\]](#)
18. Han, B.O.; Lavernia, E.J.; Lee, Z.; Nutt, S.; Witkin, D. Deformation behavior of bimodal nanostructured 5083 Al alloys. *Metall. Mat. Trans. A* **2005**, *36*, 957–965. [\[CrossRef\]](#)
19. Ye, J.; Han, B.Q.; Lee, Z.; Ahn, B.; Nutt, S.R.; Schoenung, J.M. A tri-modal aluminum based composite with super-high strength. *Scr. Mater.* **2005**, *53*, 481–486. [\[CrossRef\]](#)

20. Taya, M.; Lulay, K.E.; Lloyd, D.J. Strengthening of a particulate metal matrix composite by quenching. *Acta Metall. Mater.* **1991**, *39*, 73–87. [[CrossRef](#)]
21. Casati, R.; Fabrizi, A.; Timelli, G.; Tuissi, A.; Vedani, M. Microstructural and mechanical properties of Al-based composites reinforced with in-situ and ex-situ Al₂O₃ nanoparticles. *Adv. Eng. Mater.* **2016**, *18*, 550–558. [[CrossRef](#)]
22. Lubyanskiy, Y.V.; Bondarev, A.D.; Soshnikov, I.P.; Bert, N.A.; Zolotarev, V.V.; Kirilenko, D.A.; Kotlyar, K.P.; Pikhtin, N.A.; Tarasov, I.S. Oxygen nitrogen mixture effect on aluminum nitride synthesis by reactive ion plasma deposition. *Semiconductors* **2018**, *52*, 184–188. [[CrossRef](#)]
23. Kutzhanov, M.K.; Matveev, A.T.; Bondarev, A.V.; Polcar, T.; Duchoň, J.; Shtansky, D.V. Al-based composites reinforced with ceramic particles formed by in situ reactions between Al and amorphous SiN_xO_y. *Mater. Sci. Eng. A* **2022**, *842*, 143105. [[CrossRef](#)]
24. Casati, R.; Fabrizi, A.; Tuissi, A.; Xia, K.; Vedani, M. ECAP consolidation of Al matrix composites reinforced with in-situ γ -Al₂O₃ nanoparticles. *Mater. Sci. Eng. A* **2015**, *648*, 113–122. [[CrossRef](#)]
25. Esmaeily, A.S.; Mills, S.; Coey, J.M.D. Exceptional room-temperature plasticity in amorphous alumina nanotubes fabricated by magnetic hard anodization. *Nanoscale* **2017**, *9*, 5205–5211. [[CrossRef](#)]
26. Balog, M.; Hu, T.; Krizik, P.; Riglos, M.V.C.; Saller, B.D.; Yang, H.; Schoenung, J.M.; Lavernia, E.J. On the thermal stability of ultrafine-grained Al stabilized by in-situ amorphous Al₂O₃ network. *Mater. Sci. Eng. A* **2015**, *648*, 61–71. [[CrossRef](#)]
27. Liu, X.; Li, J.; Liu, E.; Li, Q.; He, C.; Shi, C.; Zhao, N. Synergistic strengthening effect of alumina anchored graphene nanosheets hybrid structure in aluminum matrix composites. *Fuller. Nanotub. Carbon Nanostructures* **2019**, *27*, 640–649. [[CrossRef](#)]
28. Sadeghi, B.; Cavaliere, P.; Balog, M.; Pruncu, C.I.; Shabani, A. Microstructure dependent dislocation density evolution in micro-macro rolled Al₂O₃/Al laminated composite. *Mater. Sci. Eng. A* **2022**, *830*, 142317. [[CrossRef](#)]
29. Singh, T.; Tiwari, S.K.; Shukla, D.K. Effects of Al₂O₃ nanoparticles volume fractions on microstructural and mechanical characteristics of friction stir welded nanocomposites. *Nanocomposites* **2020**, *6*, 76–84. [[CrossRef](#)]
30. Leparoux, M.; Kollo, L.; Kwon, H.; Kallip, K.; Babu, N.K.; AlOgab, K.; Talari, M.K. Solid state processing of aluminum matrix composites reinforced with nanoparticulate materials. *Adv. Eng. Mater.* **2018**, *20*, 1800401. [[CrossRef](#)]
31. Krizik, P.; Balog, M.; Nagy, S. Small punch testing of heat resistant ultrafine-grained Al composites stabilized by nano-metric Al₂O₃ (HITEMAL©) in a broad temperature range. *J. Alloys Compd.* **2021**, *887*, 161332. [[CrossRef](#)]
32. Zaiemyekheh, Z.; Liaghat, G.H.; Ahmadi, H.; Khan, M.K.; Razmkhah, O. Effect of strain rate on deformation behavior of aluminum matrix composites with Al₂O₃ nanoparticles. *Mater. Sci. Eng. A* **2019**, *753*, 276–284. [[CrossRef](#)]
33. Vogel, T.; Ma, S.; Liu, Y.; Guo, Q.; Zhang, D. Impact of alumina content and morphology on the mechanical properties of bulk nanolaminated Al₂O₃-Al composites. *Compos. Commun.* **2020**, *22*, 100462. [[CrossRef](#)]
34. Reddy, M.P.; Ubaid, F.; Shakoor, R.A.; Parande, G.; Manakari, V.; Mohamed, A.M.A.; Gupta, M. Effect of reinforcement concentration on the properties of hot extruded Al-Al₂O₃ composites synthesized through microwave sintering process. *Mater. Sci. Eng. A* **2017**, *696*, 60–69. [[CrossRef](#)]
35. Hilditch, T.B.; de Souza, T.; Hodgson, P.D. Properties and automotive applications of advanced high-strength steels (AHSS). In *Welding and Joining of Advanced High Strength Steels (AHSS)*; Shome, M., Tumuluru, M., Eds.; Woodhead Publishing: Sawston, UK, 2015; pp. 9–28. [[CrossRef](#)]
36. Balog, M.; Krizik, P.; Yan, M.; Simancik, F.; Schaffer, G.B.; Qian, M. SAP-like ultrafine-grained Al composites dispersion strengthened with nanometric AlN. *Mater. Sci. Eng. A* **2013**, *588*, 181–187. [[CrossRef](#)]
37. Pan, L.; Zhang, S.; Yang, Y.; Gupta, N.; Yang, C.; Zhao, Y.; Hu, Z. High-temperature mechanical properties of aluminum alloy matrix composites reinforced with Zr and Ni trialuminides synthesized by in situ reaction. *Metall. Mater. Trans. A* **2020**, *51*, 214–225. [[CrossRef](#)]
38. Corthay, S.; Firestein, K.L.; Kvashnin, D.G.; Kutzhanov, M.K.; Matveev, A.T.; Kovalskii, A.M.; Leybo, D.V.; Golberg, D.V.; Shtansky, D.V. Elevated-temperature high-strength h-BN-doped Al2014 and Al7075 composites: Experimental and theoretical insights. *Mater. Sci. Eng. A* **2021**, *809*, 140969. [[CrossRef](#)]
39. Summers, P.T.; Chen, Y.; Rippe, C.M.; Allen, B.; Mouritz, A.P.; Case, S.W.; Lattimer, B.Y. Overview of aluminum alloy mechanical properties during and after fires. *Fire Sci. Rev.* **2015**, *4*, 3. [[CrossRef](#)]
40. Valiev, R.Z.; Murashkin, M.Y.; Sabirov, I. A nanostructural design to produce high-strength Al alloys with enhanced electrical conductivity. *Scr. Mater.* **2014**, *76*, 13–16. [[CrossRef](#)]
41. Senkova, S.V.; Senkov, O.N.; Miracle, D.B. Cryogenic and elevated temperature strengths of an Al–Zn–Mg–Cu alloy modified with Sc and Zr. *Metall. Mater. Trans. A* **2006**, *37*, 3569–3575. [[CrossRef](#)]
42. Inoue, A.; Kimura, H. High-strength aluminum alloys containing nanoquasicrystalline particles. *Mater. Sci. Eng. A* **2000**, *286*, 1–10. [[CrossRef](#)]
43. Pickens, J.R. High-strength aluminum P/M alloys. In *ASM Handbook Committee*; ASM: Almere, The Netherlands, 1990; Volume 2, pp. 200–215.
44. Ma, X.; Zhao, Y.F.; Tian, W.J.; Qian, Z.; Chen, H.W.; Wu, Y.Y.; Liu, X.F. A novel Al matrix composite reinforced by nano-AlNp network. *Sci. Rep.* **2016**, *6*, 34919. [[CrossRef](#)] [[PubMed](#)]
45. Firestein, K.L.; Corthay, S.; Steinman, A.E.; Matveev, A.T.; Kovalskii, A.M.; Sukhorukova, I.V.; Golberg, D.; Shtansky, D.V. High-strength aluminum-based composites reinforced with BN, AlB₂ and AlN particles fabricated via reactive spark plasma sintering of Al-BN powder mixtures. *Mater. Sci. Eng. A* **2017**, *681*, 1–9. [[CrossRef](#)]

46. Kutzhanov, M.K.; Matveev, A.T.; Kvashnin, D.G.; Corthay, S.; Jalolov, F.N.; Kvashnin, A.G.; Konopatsky, A.S.; Leybo, D.V.; Bondarev, A.V.; Arkhipova, N.A.; et al. Al/SiC composites with enhanced thermomechanical properties obtained from microwave plasma-treated nanopowders. *Mater. Sci. Eng. A* **2021**, *824*, 141817. [[CrossRef](#)]
47. Baek, M.-S.; Euh, K.; Lee, K.-A. Microstructure, tensile and fatigue properties of high strength Al 7075 alloy manufactured via twin-roll strip casting. *J. Mater. Res. Technol.* **2020**, *9*, 9941–9950. [[CrossRef](#)]
48. Zhao, J.; Jiang, Z. Thermomechanical processing of advanced high strength steels. *Progress Mater. Sci.* **2018**, *94*, 174–242. [[CrossRef](#)]
49. Zhu, Y.T.; Liao, X.Z.; Wu, X.L. Deformation twinning in nanocrystalline materials. *Prog. Mater. Sci.* **2012**, *57*, 1–62. [[CrossRef](#)]
50. Kou, Z.; Yang, Y.; Yang, L.; Zhang, W.; Huang, B.; Luo, X. Deformation twinning in response to cracking in Al: An in situ TEM and molecular dynamics study. *Scripta Mater.* **2018**, *145*, 28–32. [[CrossRef](#)]
51. Goswami, R.; Pande, C.S.; Bernstein, N.; Johannes, M.D.; Baker, C.; Villalobos, G. A high degree of enhancement of strength of sputter deposited Al/Al₂O₃ multilayers upon post annealing. *Acta Mater.* **2015**, *95*, 378–385. [[CrossRef](#)]

Disclaimer/Publisher’s Note: The statements, opinions and data contained in all publications are solely those of the individual author(s) and contributor(s) and not of MDPI and/or the editor(s). MDPI and/or the editor(s) disclaim responsibility for any injury to people or property resulting from any ideas, methods, instructions or products referred to in the content.